RSC Advances

PAPER

View Article Online
View Journal | View Issue

Cite this: *RSC Adv.*, 2021, **11**, 3981

Upconversion luminescence and temperature sensing properties of $NaGd(WO_4)_2:Yb^{3+}/Er^{3+}@SiO_2$ core–shell nanoparticles†

Lu Zheng,[a] Xinyi Huang,[a] Jiuping Zhong,[*a] Zijun Wang[b] and Xiaoning Cheng[c]

Optical thermometry based on the fluorescence intensity ratio (FIR) of two thermally coupled levels in lanthanide ions has potential application in non-contact optical temperature sensing techniques. In this work, a shell of SiO_2 with tunable thickness was uniformly coated on $NaGd(WO_4)_2:Yb^{3+}/Er^{3+}$ core upconversion nanoparticles (UCNPs). The effects of the silica shell on UC luminescence and thermal sensing properties of core–shell $NaGd(WO_4)_2:Yb^{3+}/Er^{3+}@SiO_2$ UCNPs were investigated. Under 980 nm laser excitation, the temperature-dependent UC emission spectra of obtained samples were measured. The FIR was analyzed based on the thermally coupled $^2H_{11/2}$ and $^4S_{3/2}$ levels of Er^{3+} in the biological temperature range of 300–350 K, in which the Boltzmann distribution is applied. The emission from the upper $^2H_{11/2}$ state within Er^{3+} was enhanced as temperature increased due to the thermal effect. Absolute sensitivities (S_A) and relative sensitivities (S_R) of the core and core–shell UCNPs were calculated. It was found that after SiO_2 coating, the maximum S_A was enhanced by ~2-fold (1.03% K^{-1} at 350 K). Especially, S_A was as high as 2.14% K^{-1} at 350 K by analyzing the FIR of the non-thermally coupled $^2H_{11/2}$ and $^4F_{9/2}$ levels.

Received 27th November 2020
Accepted 5th January 2021

DOI: 10.1039/d0ra10039k

rsc.li/rsc-advances

1. Introduction

Lanthanide-doped nanomaterials have been widely investigated in bio-therapies, such as magnetic resonance imaging, photodynamic therapy, photothermal therapy, and X-ray tomography because of their outstanding chemical and optical properties.[1–5] In biological environments, temperature is an important parameter. However, it is not easy to get accurate temperature *in vivo* directly. Recently, upconversion (UC) luminescent materials for optical temperature sensing application have been received considerable attention.[6] It is based on the fluorescence intensity ratio (FIR) of two thermally coupled energy levels, which can provide a non-invasive technique to monitoring temperature with a high sensitivity and a fast response. This technique is independent on variations of sample concentration and intensity fluctuation.[7,8] The energy difference is required to be in the range of 200–2000 cm^{-1} to enable a Boltzmann distribution for the population ratio of two neighboring excited states.[9] The Yb^{3+} and Er^{3+} ions are the most popular ion couple to realize UC luminescence. The $^2H_{11/2}$ and $^4S_{3/2}$ levels within Er^{3+} are thermally coupled with energy gap of ~800 cm^{-1}. Yb^{3+} ions are employed as the co-doping ions to sensitize Er^{3+} due to the large absorption cross-section at 980 nm of Yb^{3+} and the efficient energy transfer from Yb^{3+} to Er^{3+}.

Compounds such as oxides, fluorides, and oxysulfides, have been reported with good properties of optical temperature sensing.[10,11] However, to enable good control of shape and uniformity, UC nanoparticles (UCNPs) are usually synthesized in non-polar solvents. Then, aqueous dispersibility is absent for the UCNPs. Therefore, post-treatments are usually required.[12] In general, rare-earth oxides have better thermal stability and thermal sensitivity than fluorides,[13–15] and thus are promising in bio-imaging and bio-sensing. Coating the nanoparticles with shell structures is a common approach to eliminate the surface defects and enhance the luminescence, so the optical thermometry performance of the nanoparticles can be improved.[16–18] A versatile shell is silica due to its high chemical stability, optical transparency, and easy control of shell thickness. Especially, for biological applications, the silica is non-toxic and bio-compatible,[19,20] and the surface of the silica can be further modified to enable dispersity in a variety of polar solvents.[21] The silica can be porous and can realize targeting binding, such as for drug delivering.[22–25] Therefore, SiO_2 coating on lanthanide doped nanomaterials can not only improve the chemical and physical properties, but expand the application of lanthanide doped luminescent materials in biomedicine fields.

Lanthanide doped double tungstates have been investigated as potential thermometric probes due to their good thermal stability

[a]School of Materials, Sun Yat-sen University, Guangzhou 510275, China. E-mail: zhongjp@mail.sysu.edu.cn

[b]Laboratoire de Physique de la Matière Condensée, Ecole Polytechnique, CNRS, IP Paris, Palaiseau, 91128, France

[c]Instrumental Analysis & Research Center, Sun Yat-sen University, Guangzhou 510275, China

† Electronic supplementary information (ESI) available. See DOI: 10.1039/d0ra10039k

and high thermal sensitivity.[26–28] Temperature sensing performance of material can be improved after silica coating. It has been reported that the performing temperature of nanothermometry for the classical up-converting nanoparticles $NaYF_4$:Er^{3+},Yb^{3+} was expanded from 600 K to 900 K, which enables the application of the material in high temperature environments.[29] The protective effect of silica shell benefits the UCNPs to maintain the morphology and optical properties at high temperatures with good repeatability. In addition, the UC luminescence and the thermal sensitivity can be enhanced by the silica coating, which was demonstrated by the study on $LuVO_4$:Yb^{3+}/Er^{3+}.[30]

In this work, $NaGd(WO_4)_2$:Yb^{3+}/Er^{3+} (NGW:Yb^{3+}/Er^{3+}) core UCNPs and $NaGd(WO_4)_2$:Yb^{3+}/Er^{3+}@SiO_2 (NGW:Yb^{3+}/Er^{3+}@SiO_2) core–shell UCNPs were successfully synthesized. Silica with different thickness was coated on NGW:Yb^{3+}/Er^{3+} nanoparticles by Stöber method. The morphology, structure and luminescence properties of the core NGW:Yb^{3+}/Er^{3+} and core–shell NGW:Yb^{3+}/Er^{3+}@SiO_2 UCNPs were characterized. Performance of optical temperature sensing was studied *via* the FIR analysis on the two thermally coupled energy levels $^2H_{11/2}$ and $^4S_{3/2}$ within Er^{3+}. The benefits of silica shell coating were also discussed in detail.

2. Experimental

2.1 Materials

Absolute ethanol (Analytical Reagent, A.R.), ammonium hydroxide (A.R.), gadolinium(III) acetate hydrate (99.9%), ytterbium(III) acetate hydrate (99.9%), erbium(III) acetate hydrate (99.9%), sodium tungstate hydrate (A.R.), ethylene glycol (A.R.), tetraethyl orthosilicate (TEOS, 99.0%) were used as raw materials without further purification.

2.2 Synthesis of NGW:Yb^{3+}/Er^{3+} UCNPs

NGW:Yb^{3+}/Er^{3+} core UCNPs were synthesized with ethylene glycol-assistant hydrothermal method. Firstly, solutions of 0.10 mol L^{-1} $Gd(CH_3COOH)_3$, 0.10 mol L^{-1} $Yb(CH_3COOH)_3$, 0.02 mol L^{-1} $Er(CH_3COOH)_3$ and 0.20 mol L^{-1} Na_2WO_4 were prepared *via* dissolving the reactants separately in deionized water. Next, 3.33 mL Na_2WO_4 was added to the solution containing 2.65 mL $Gd(CH_3COOH)_3$, 0.67 mL $Yb(CH_3COOH)_3$ and 83 μL $Er(CH_3COOH)_3$ under magnetic stirring. After stirring for 5 min, 27 mL ethylene glycol was mixed into the solution with following vigorous stirring for 30 min. Subsequently, the mixture was transferred into a 40 mL Teflon-lined stainless autoclave, which was sealed and maintained at 200 °C for 20 h. The white products were collected by centrifugation and washed three times with distilled water and ethanol, and were obtained in powder after drying at 70 °C for 12 h. Finally, the obtained UCNPs were annealed at 600 °C for 3 h with temperature rise of 2 °C min^{-1} in a muffle furnace.

2.3 Synthesis of NGW:Yb^{3+}/Er^{3+}@SiO_2 UCNPs

In order to coat a SiO_2 shell onto the NGW:Yb^{3+}/Er^{3+} UCNPs, 0.030 g NGW:Yb^{3+}/Er^{3+} UCNPs were dispersed in mixtures including 50 mL ethanol, 10 mL deionized water, and 2 mL ammonium hydroxide in a 100 mL flask *via* ultrasonication for 20 min. Then, TEOS dropwise was added with mild stirring. To prepare core–shell UCNPs with various SiO_2 shell thickness, a certain amount of TEOS (10 μL, 20 μL, 40 μL, 80 μL, 160 μL and 320 μL) was added into the above mentioned solution with stirring at room temperature for 8 h. The suspensions were washed by deionized water and ethanol for three times, and the NGW:Yb^{3+}/Er^{3+}@SiO_2 UCNPs were collected by centrifugation and further dried at 70 °C for 12 h. Finally, the obtained UCNPs were annealed at 600 °C for 3 h with a heating rate of 2 °C min^{-1} in a muffle furnace.

2.4 Characterization

Crystal phase of the prepared UCNPs was determined by X-ray diffractometer (XRD, RIGAKU, D-MAX 2200 VPC, Cu Kα radiation) at a scanning rate of 10° min^{-1} with a step of 0.02° and 2θ ranging from 10° to 70°. Fourier transform infrared (FT-IR, Frontier) spectra were measured within the frequency range of 400–4000 cm^{-1} by using the KBr pellet technique. Morphologies of UCNPs were characterized by scanning electron microscope (SEM, field-emission SEM, Zeiss Gemini 500) with an energy dispersive X-ray spectrometer (EDS, Bruker Flat QUAD). High-Resolution Transmission Electron Microscopies (HRTEM) were analyzed by using spherical aberration corrected transmission electron microscope JEM-ARM200P. UC emission spectra and decay curves at room temperature were obtained using the Edinburgh Instruments FLS1000 spectrometer with a power tunable 980 nm laser as the excitation light source and a detector of photomultiplier tube (Hamamatsu R928P). Temperature-dependent UC emission spectra were measured using the OXFORD instrument with a temperature controlling system under nitrogen cryogenics.

3. Results and discussion

3.1 Crystal structure and morphologies

The synthetic procedures of core NGW:Yb^{3+}/Er^{3+} and core–shell NGW:Yb^{3+}/Er^{3+}@SiO_2 UCNPs are schematically shown in Fig. 1a. The core UCNPs were synthesized initially by the hydrothermal method. Then, the tunable silica layers were coated on the core NGW:Yb^{3+}/Er^{3+} UCNPs by the Stöber method. Finally, both the core and core–shell UCNPs were sintered in air at 600 °C for 3 h to improve the crystallinity and enhance the luminescence properties.

The $NaGd(WO_4)_2$ crystal is in a scheelite-like tetragonal structure with $I4_1/a$ space group and cell parameters of $a = b =$ 0.5243 nm, $c = 1.1368$ nm.[31] The phase composition and crystalline nature of the prepared samples at each stage have been characterized by XRD measurements. Fig. 1b shows the XRD patterns of the core and core–shell UCNPs. Referring to the $NaGd(WO_4)_2$ standard (JCPDS#25-0829), both the core and core–shell UCNPs are in the tetragonal structure. No second diffraction peak can be observed after the silica coating.

The surface chemistry of the core NGW:Yb^{3+}/Er^{3+} and core–shell NGW:Yb^{3+}/Er^{3+}@SiO_2 UCNPs were analyzed by FT-IR measurements as shown in Fig. 1c. The multiple absorption peaks from 700 cm^{-1} to 900 cm^{-1} and weak absorption band

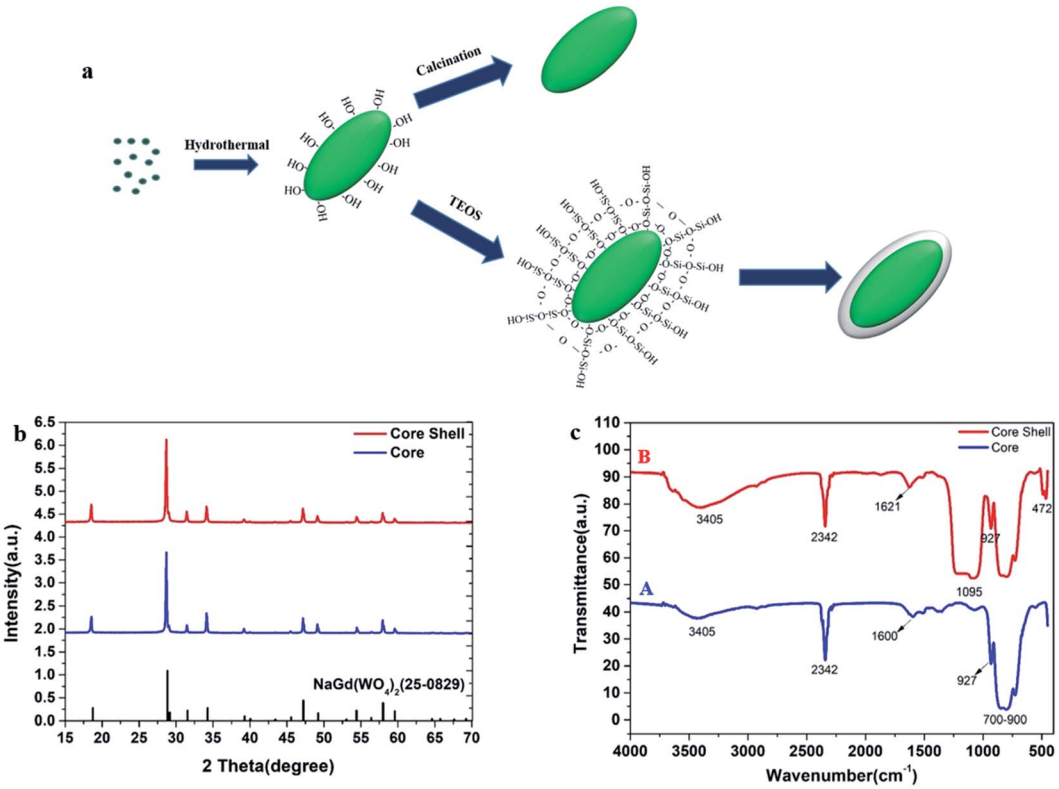

Fig. 1 Characterizations for the core NGW:Yb^{3+}/Er^{3+} and the core–shell NGW:Yb^{3+}/Er^{3+}@SiO_2 UCNPs after annealing. (a) Schematic illustration for the synthesis. (b) XRD patterns. (c) FT-IR spectra.

around 927 cm^{-1} are assigned to the asymmetrical stretching vibrations and symmetrical stretching vibrations of W–O in the WO_4^{2-} group.[32,33] The peak around 2342 cm^{-1} observed in both UCNPs is due to the asymmetrical C–O stretching mode from ambient of CO_2.[34] In addition, the broad absorption bands near 3405 cm^{-1} and 1600 cm^{-1} can be attributed to the O–H stretching and bending vibrations of water molecules, respectively. The water adsorption on the UCNPs can occur during the preparation of the UCNPs, especially because the UCNPs are nanocrystalline. The new peaks at 1095 cm^{-1} and 472 cm^{-1} (curve B) belong to the symmetrical stretching vibration of Si–O–Si and the bending vibration of Si–O, which indicates the successful coating of silica shell.

To explore the direct formation of the silica layer around the NGW:Yb^{3+}/Er^{3+} UCNPs, scanning transmission electron microscopy in scanning electron microscopy (STEM-in-SEM) was used to determine the morphology of the products in different stages as shown in Fig. 2. Core NGW:Yb^{3+}/Er^{3+} UCNPs are monodisperse in a regular olivary shape with an average size of 300 nm × 150 nm (Fig. 2a). We can observe the distinct contrast between the core and the shell structures. The low contrast contour demonstrates a uniform growth of the silica shell on the core NGW:Yb^{3+}/Er^{3+} UCNPs. The mean thickness of silicon shell is 25 nm (Fig. 2c). The morphology and monodispersity for the UCNPs are unaltered after the SiO_2 coating. Therefore, the STEM images confirm that the NGW:Yb^{3+}/Er^{3+} UCNPs are coated by silica shell successfully.

Lattice fringes can be well-resolved in the HR-TEM image (Fig. 2d) and the distance of lattice fringe is 0.310 nm, which is consistent with the d-spacing between (112) planes of $NaGd(WO_4)_2$ (JCPDS#25-0829). The inset in Fig. 2d is the corresponding fast Fourier transform pattern, indicating a single crystalline nature of the inner core $NaGd(WO_4)_2$. Moreover, the EDS spectra and elemental mapping profile of the core–shell UCNPs (Fig. 2e and f) were collected through a single core–shell UCNP to qualitatively analyze the chemical compositions. The resulting elemental mapping profile in Fig. 2f reveals the homogeneous distribution of Na, Gd, W, Si, O in the core–shell UCNPs. Notice that the Si and O elements (red and indigo) cover larger area than other elements, which confirms the existence of the silicon outer shell.

For biological nanomaterial, it is imperative to produce UCNPs with good control on morphology, size, and aqueous dispersity. To give an insight into the effects of SiO_2 shell on morphology and monodispersity, the obtained core and core–shell UCNPs before and after annealing are characterized by STEM as showed in Fig. S1.† The core NGW:Yb^{3+}/Er^{3+} UCNPs are well-dispersed in water after the hydrothermal reaction. However, the annealing process, which is used to improve the luminescence properties of the UCNPs, could cause a severe agglomeration (see Fig. S1b†). This problem can be solved mostly by coating SiO_2 shell, as shown in Fig. S1c.† Due to the protective effect of the silica, the NGW Yb^{3+}/Er^{3+}@SiO_2 core–shell UCNPs after annealing preserve the morphology and the monodispersity. In addition, the thickness of SiO_2 layer can be tuned by changing the amount of TEOS that is the silica source during the shell growth. The STEM images of the NGW Yb^{3+}/Er^{3+}@SiO_2 core–shell UCNPs with silica layer in different

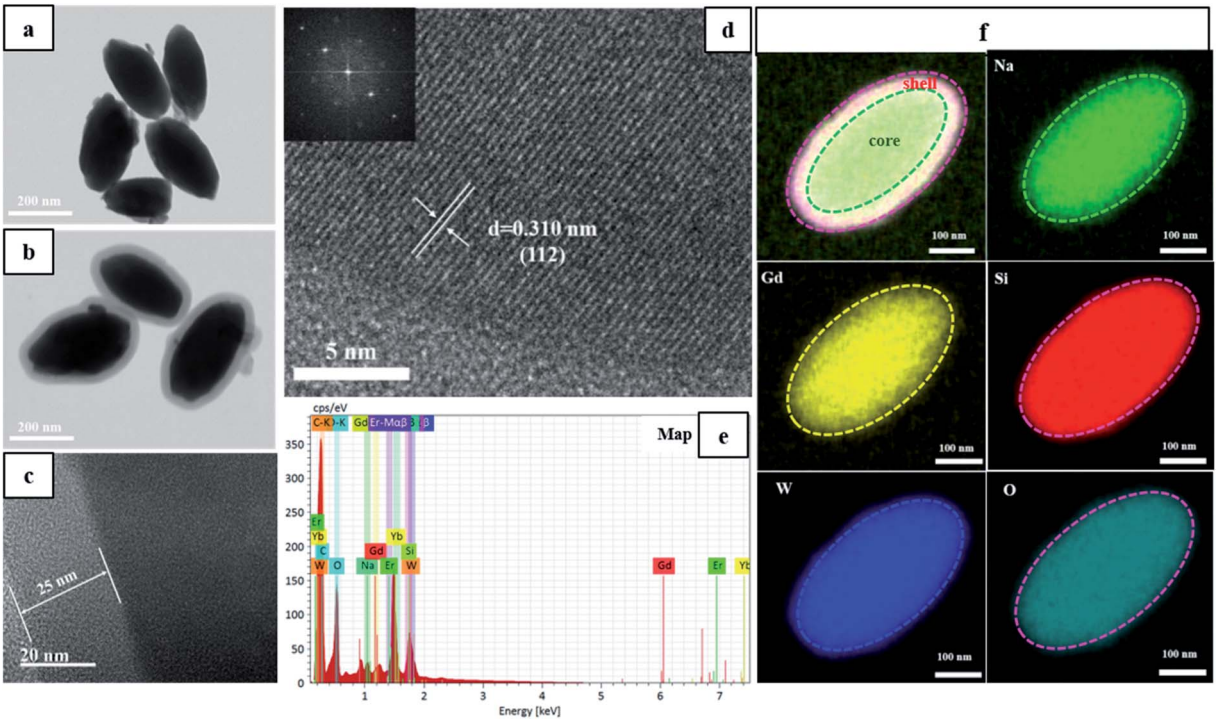

Fig. 2 Electron microscopy characterizations of the core NGW:Yb^{3+}/Er^{3+} and the core–shell NGW Yb^{3+}/Er^{3+}@SiO_2 UCNPs. (a and b) STEM images. (c and d) HR-TEM images. (e) EDS spectrum. (f) Elemental mapping profiles.

thickness are shown in Fig. S2.† The average thickness of SiO_2 layer is calculated to be 15 nm, 25 nm, 40 nm, 60 nm, 90 nm, 120 nm for the UCNPs synthesized with 10 μL, 20 μL, 40 μL, 80 μL, 160 μL, and 320 μL TEOS. If the TEOS is much excess, spherical silica can be formed as a second phase (Fig. S2f†).

3.2 Upconversion luminescence properties and mechanism

To investigate the effect of the silica shell on UC emission, the UC spectra of the core (NGW:Yb^{3+}/Er^{3+}) and core–shell (NGW:Yb^{3+}/Er^{3+}@SiO_2) UCNPs were measured under excitation of 980 nm laser (power density of 56 mW cm^{-2}). The optimal doping concentrations for Yb^{3+}/Er^{3+} ions are 20% Yb^{3+} and 0.5% Er^{3+} according to the analysis of concentration quenching (Figure S3†). As shown in Fig. 3a, the UC emission consists of intra-configurational 4f–4f Er^{3+} transitions at green and red regions. The red emission with maximum intensity at 657 nm derives from the $^4F_{9/2} \rightarrow {}^4I_{15/2}$ transition. The green emission is attributed to the transitions from the thermally coupled states $^2H_{11/2}$ and $^4S_{3/2}$ to the ground state $^4I_{15/2}$ at 531.5 nm and 553 nm. The silica shell has no influence on the position of emission lines and the relative UC emission intensity. For nanoparticles, on the one hand, UC luminescence can be enhanced by growth of SiO_2 shell owning to the passivation effect to reduce the surface defects.[35–38] On the other hand, SiO_2 layers can quench the UC emission due to O–H vibrations. As our UCNPs before and after silica coating are thermally treated, the above effects of silica coating can be neglected. As a result, the core–shell UCNPs are similar to the core UCNPs on the UC luminescence intensity.

In the Yb^{3+}–Er^{3+} ion couple, Yb^{3+} ions can resonantly transfer energy to neighboring Er^{3+} ions involving a multi-photon process. UC emission spectra were measured under different excitation powder density of laser. The relation of UC emission intensity and pumping power density can be described by eqn (1):

$$I_{UC} = P_{pump}{}^{n} \quad (1)$$

where I is the UC emission intensity, P represents the 980 nm laser power density, and value n is the number of pumped IR photons that are required for UC emission. The logarithm of UC emission intensity is plotted *versus* power in Fig. 3b, indicating a two-photon UC process for the red emission. Both two- and three-photon UC processes contribute to the green emission. The silica shell barely affects the UC processes. The energy level diagram and the proposed energy transfer UC mechanism are schematically shown in Fig. 3c. Upon excitation of 980 nm laser, the Yb^{3+} ions are excited from the ground state $^2F_{7/2}$ to the excited state $^2F_{5/2}$. Energy could be resonantly transferred from Yb^{3+} excited state to Er^{3+} $^4I_{11/2}$ by ground state absorption. The Er^{3+} ion is excited to the $^4F_{7/2}$ excited state by subsequent excited state absorption. Fast non-radiative relaxation occurs from $^4F_{7/2}$ to $^2H_{11/2}$, $^4S_{3/2}$ or $^4F_{9/2}$ states. An alternative path to populate the red emission state is originated from the nonradiative relaxation from $^4I_{11/2}$ to $^4I_{13/2}$ and the following excited state absorption. From the red emitting $^4F_{9/2}$ level, a third photon can be absorbed and excites Er^{3+} to $^2H_{9/2}$ state. Finally, the radiative decay from the excited states $^2H_{11/2}$, $^4S_{3/2}$ and $^4F_{9/2}$ to the ground state $^4I_{15/2}$ gives rise to green and red emission.

Fig. 4a and b shows the luminescence decay curves of the $^2H_{11/2}/{}^4S_{3/2}$ and $^4F_{9/2}$ excited states for both core and core–shell UCNPs. The rise time indicates the energy transfer of Yb^{3+} to Er^{3+} ions. Following decay fits to the mono-exponential

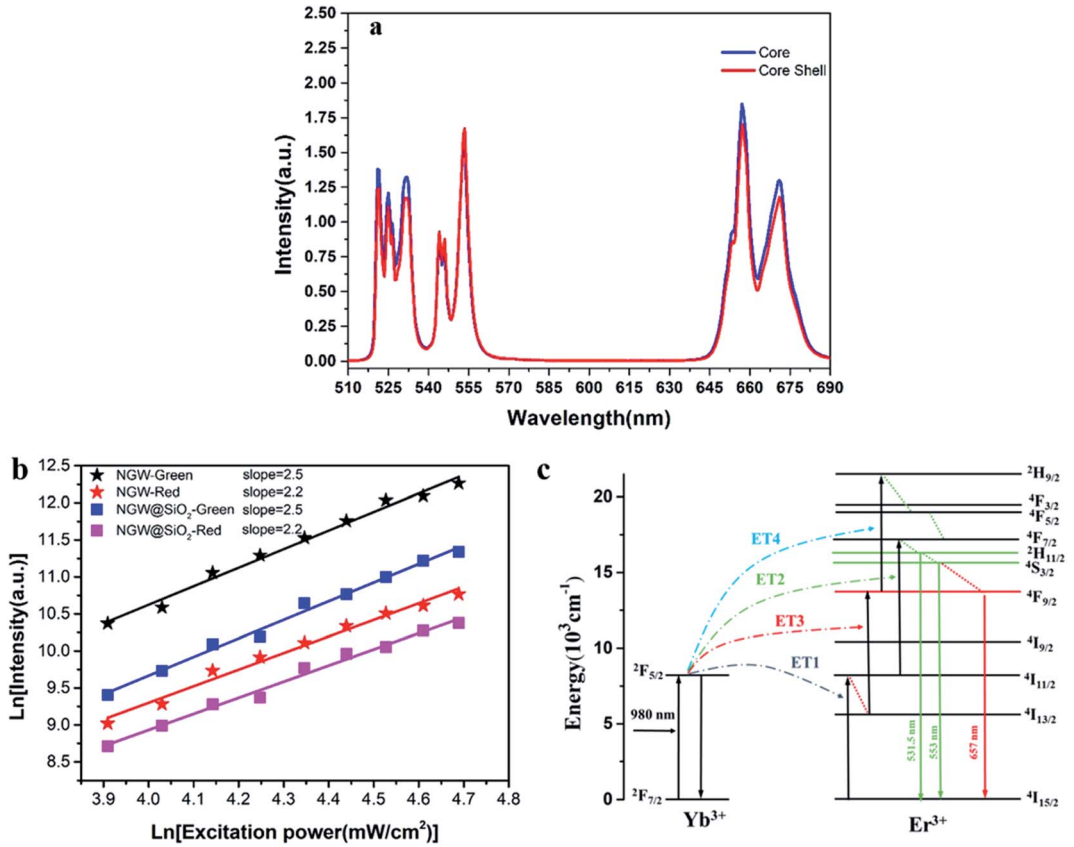

Fig. 3 (a) UC emission spectra for the core NGW:Yb^{3+}/Er^{3+} and the core–shell NGW Yb^{3+}/Er^{3+}@SiO_2 UCNPs under excitation of 980 nm laser (power density of 56 mW cm^{-2}). (b) Double logarithmic plot of green and red UC emission intensity *versus* excitation power density for the core and core–shell UCNPs. The solid lines are the linear fits of the double logarithmic plots. (c) Energy-level diagram for UC emission.

behavior. The lifetime for the $^2H_{11/2}/^4S_{3/2}$ green UC emission is 40.2 μs (core) and 40.7 μs (core–shell). For the $^4F_{9/2}$ red emission, the lifetime is 68.4 μs (core) and 66.6 μs (core–shell). Again, the results of decay time confirm that UC emission and UC efficiency is unaltered with the silica coating. The decay time of the green and the red UC emission is 2–3 times longer than those for $NaY(WO_4)_2$:Er^{3+}/Yb^{3+} UCNPs in our previous work.[39] Reason is that the UCNPs in this work is relatively large in size and is thermally treated, thus the quenching from defects and surrounding ligands is largely suppressed.

To further justify the effects of the silica coating on UC luminescence, the NGW:Yb^{3+}/Er^{3+} core UCNPs were coated with a silica shell in varied thickness. The UC emission spectra for these core–shell UCNPs (Fig. S4†) show that the UC emission intensity decreases gradually upon coating thicker layer of silica. It was speculated that the silica could attenuate the emission. The integrated intensity ratio of green and red emission is plotted in Fig. S4.† With the increased silica shell, the integrated intensity ratio of green/red emission increases. This is contrary to the usual observation of enhanced red emission, thus decreased green/red intensity

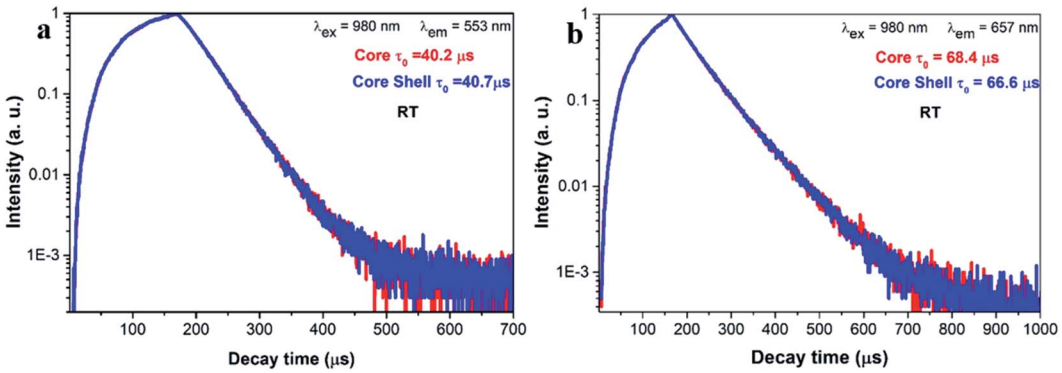

Fig. 4 Luminescence decay of (a) $^2H_{11/2}/^4S_{3/2}$ green emission and (b) $^4F_{9/2}$ red emission for the core NGW:Yb^{3+}/Er^{3+} and the core–shell NGW Yb^{3+}/Er^{3+}@SiO_2 UCNPs under excitation of 980 nm laser (power density of 56 mW cm^{-1-2}).

ratio.[35,40] In those cases, the nonradiative decay from Er^{3+} $^4I_{11/2}$ to $^4I_{13/2}$ state is enhanced due to the O–H quenching as the energy gap between $^4I_{11/2}$ and $^4I_{13/2}$ states matches the O–H vibration energy (3200–2600 cm^{-1}).[41,42] Then, there is a high probability that the second IR photon excites Er^{3+} from the $^4I_{13/2}$ state to the red emitting $^4F_{9/2}$ state. In our case, the core–shell UCNPs with thermal treatment are limited influenced by the O–H quenching. This agrees with the unchanged green and red emitting lifetime after the silica coating because the nonradiative decay rate is unaltered.

3.3 Luminescence thermometry

Temperature sensing properties were measured and compared for the core NGW:Yb^{3+}/Er^{3+} and core–shell NGW:Yb^{3+}/Er^{3+}@SiO_2 UCNPs. Temperature-dependent UC emission spectra of UNCP powders were collected in the temperature range of biological systems (300–350 K in a step of 5 K) under 980 nm laser excitation (power density of 162 mW cm^{-1-2}). Before measuring spectra, each temperature point holds for at least 5 min for stabilization. The thermocouple can measure the real-time temperature and compensate the caused laser heating. Furthermore, the laser power density is relatively low, thus the laser heating effect should be slight. As the population probability in the $^2H_{11/2}$ and $^4S_{3/2}$ states follows the Boltzmann's distribution, the relative emission intensity in the two states changes with temperature. The fluorescence intensity ratio (FIR) follows eqn (2)

$$\mathrm{FIR} = \frac{I_1}{I_2} = \frac{I_{531.5\ \mathrm{nm}}}{I_{553\ \mathrm{nm}}} = B\exp\left(\frac{-\Delta E}{k_B T}\right) \quad (2)$$

where $I_{531.5\ nm}$ and $I_{553\ nm}$ are the integrated UC emission intensity of the $^2H_{11/2}$ and $^4S_{3/2}$ levels, ΔE is the energy gap between the $^2H_{11/2}$ and $^4S_{3/2}$ levels, k_B is the Boltzmann's constant, T is the absolute temperature and B is a constant. Fig. 5a shows the temperature (300–350 K) dependent UC emission spectra of the core–shell NGW:Yb^{3+}/Er^{3+}@SiO_2 UCNPs with the normalized intensity of $^4S_{3/2} \rightarrow {}^4I_{15/2}$ emission. The emission intensity of the transition $^2H_{11/2} \rightarrow {}^4I_{15/2}$ increases with temperature, as expected for the thermal coupling of excited states. Thus the FIR of the $^2H_{11/2}$ and $^4S_{3/2}$ green emission increases as shown in Fig. 5b. Fitting the plot with eqn (2), ΔE between the $^2H_{11/2}$ and $^4S_{3/2}$ states is calculated to be about 845.8 cm^{-1} and matches the experimental value of 796.4 cm^{-1} determined from the emission spectra of the core and core–shell UCNPs (Fig. 3a). For temperature sensors, absolute sensitivities (S_A) and relative sensitivities (S_R) are key parameters for practical applications to evaluate the temperature sensitivity of FIR technique and are defined as following equations:

$$S_A = \frac{\partial \mathrm{FIR}}{\partial T} = \mathrm{FIR} \times \frac{\Delta E}{k_B T^2} \quad (3)$$

$$S_R = \frac{S_A}{\mathrm{FIR}} = \frac{\Delta E}{k_B T^2} \quad (4)$$

Fig. 5c and d shows the plots of S_A and S_R *versus* temperature, respectively. In the biological temperature range from 300 K to 350 K, S_A continuously increases with temperature, whereas S_R decreases. The maximum S_A is 1.03% K^{-1} at 350 K and the maximum S_R is 1.10% K^{-1} at 300 K for the core–shell

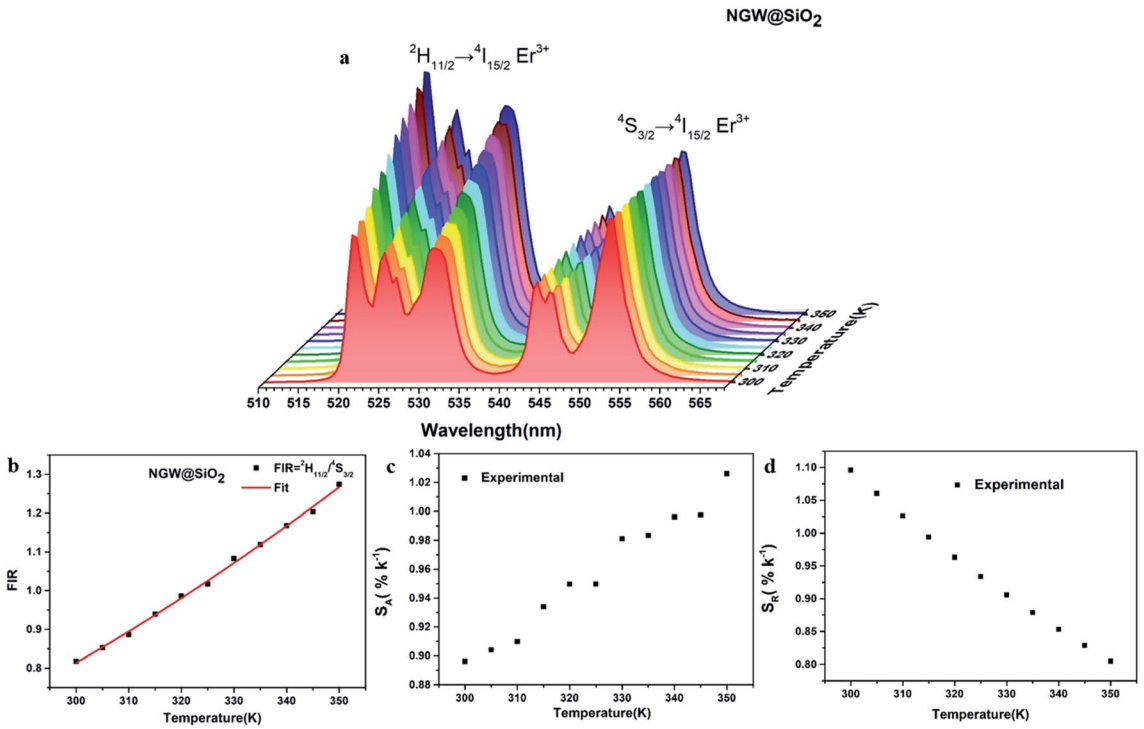

Fig. 5 FIR analysis of the $^2H_{11/2}$ and $^4S_{3/2}$ levels for the core–shell NGW:Yb^{3+}/Er^{3+}@SiO_2 UCNPs in the temperature range from 300 K to 350 K. (a) UC emission spectra under 980 nm laser excitation (power density of 162 mW cm^{-1-2}). The spectra are normalized to the emission peak at 553 nm. (b) FIR, (c) S_A, and (d) S_R *versus* temperature.

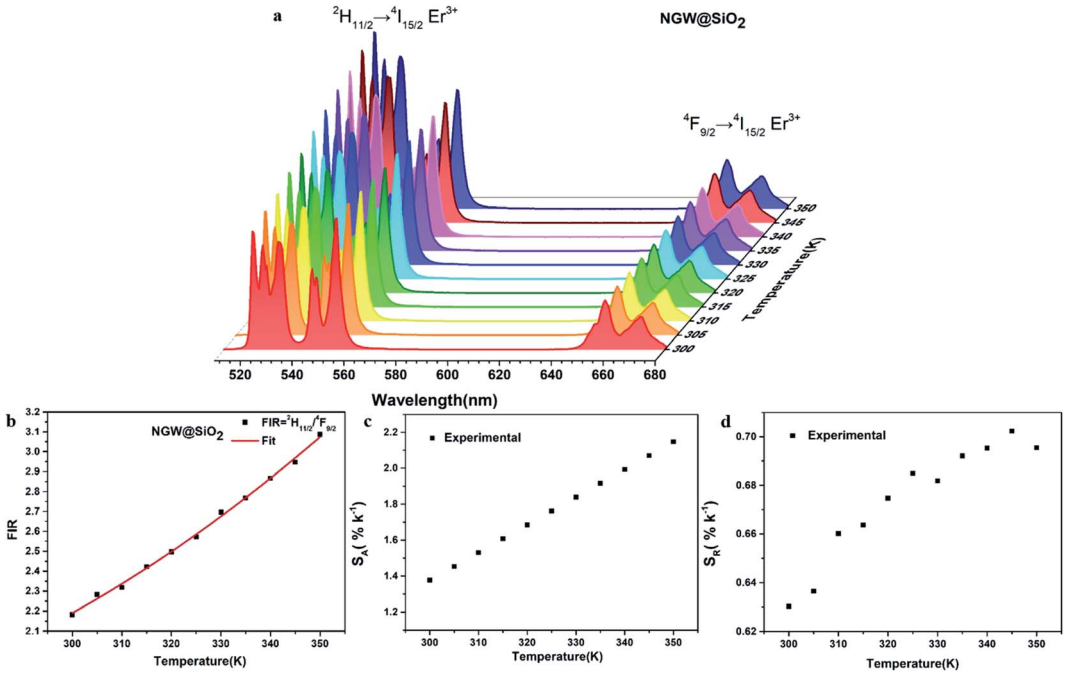

Fig. 6 FIR analysis of the $^2H_{11/2}$ green emission to the red $^4F_{9/2}$ emission for the core–shell NGW:Yb^{3+}/Er^{3+}@SiO$_2$ UCNPs in the temperature range from 300 K to 350 K. (a) UC emission spectra under 980 nm laser excitation (power density of 162 mW cm^{-2}). The spectra are normalized to the emission peak at 657 nm. (b) FIR, (c) S_A, and (d) S_R *versus* temperature.

NGW:Yb^{3+}/Er^{3+}@SiO$_2$ UCNPs. As a comparison, the temperature-sensing properties of the core NGW:Yb^{3+}/Er^{3+} UCNPs were evaluated (Fig. S5†). The S_A of the core–shell NGW:Yb^{3+}/Er^{3+}@SiO$_2$ UCNPs is ~2-fold enhanced compared with the core NGW:Yb^{3+}/Er^{3+} UCNPs in the biological temperature range. The observation of improved thermal sensitivity after silica coating is in agreement with previous studies on the system of vanadates.[30,43] It was observed that an improvement of thermal sensitivity after silica coating, but details in the mechanism for the performance improvements is still not clear. Silica coating can improve the thermal stability for NaYF$_4$:Er^{3+},Yb^{3+} UCNPs, which may provide a hint for the enhanced thermal sensitivity with the silica coating. Although enhanced UC emission is not observed after silica coating, the silica shell can somewhat passivate the surface and thus improve the thermal sensitivity. Ultrasmall NaLa(WO$_4$)$_2$:Yb^{3+}/Er^{3+} UCNPs (sub-10 nm in size) was demonstrated to be thermally stable until ~600 K.[15] In regard of present NaGd(WO$_4$)$_2$:Yb^{3+}/Er^{3+} UCNPs in a relatively big size, it is reasonable to envisage that the silica coated UCNPs in our work can survive at higher temperatures. Besides the improvement of thermal sensitivity, the silica coating can extend the application of the material to high temperature environments.

Although the most widely used model system in UC nanothermometry is the thermally coupled neighboring states, emission from non-thermally coupled states can be feasible probes of thermal sensing. Therefore, for the core–shell UCNPs, the thermal sensing ability using the FIR of the $^2H_{11/2}$ (531.5 nm) and $^4F_{9/2}$ (657 nm) levels was further investigated. The population related to the $^2H_{11/2}$ and $^4F_{9/2}$ levels is not following the Boltzmann distribution. For example, in the cases of Nd^{3+}–Yb^{3+} and Eu^{3+}–Tb^{3+} ions couples, FIR technique can monitor the emission intensity from two different emitting ions.[44,45] The emission from two emitting levels for FIR analysis is not following the Boltzmann law, which is based on energy transfer. Fig. 6a shows the temperature dependent UC emission spectra of the core–shell NGW:Yb^{3+}/Er^{3+}@SiO$_2$ UCNPs with normalized emission intensity at 657 nm. The FIR can be fit well to a second order polynomial relationship with temperature:

$$\mathrm{FIR} = \frac{I_{531.5\ \mathrm{nm}}}{I_{657\ \mathrm{nm}}} = AT^2 + BT + C \quad (5)$$

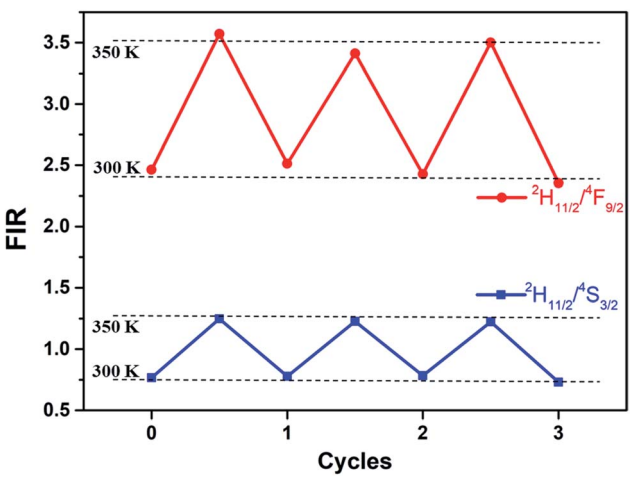

Fig. 7 FIR of Er^{3+} $^2H_{11/2}/^4S_{3/2}$ and $^2H_{11/2}/^4F_{9/2}$ at 300 and 350 K in three cycles of heating and cooling for the core–shell UCNPs (the dots are experimental data).

Table 1 Comparison of temperature-sensing properties using FIR technique within Er^{3+}

Sensing materials	Temperature range (K)	Maximum $S_A(K^{-1})$	S_R (% K^{-1})	λ (nm)	Ref.
$LuVO_4$:Yb^{3+}/Er^{3+}@SiO_2 NP	303–353	0.57% at 353 K	$1077/T^2$	525/553	46
$NaY(WO_4)_2$:Yb^{3+}/Er^{3+} NP	293–503	0.9% at 503 K	$1127/T^2$	525/552	39
$LuVO_4$:Yb^{3+}/Er^{3+} MP	303–423	0.82% at 423 K	$1030/T^2$	524/553	47
Er^{3+}/Yb^{3+}:$Na_{0.5}Gd_{0.5}MoO_4$	298–778	0.86% at 590 K	$1195/T^2$	521/541	48
β-$NaYF_4$:Yb^{3+}/Er^{3+}@SiO_2 NP	299–337	—	$1168/T^2$	525/545	49
Er^{3+}/Yb^{3+}:K_3LuF_6 MP	300–773	0.38% at 625 K	$1256/T^2$	521/545	50
Er^{3+}/Yb^{3+}:$GdVO_4$@SiO_2 NP	297–343	1.01% at 343 K	—	520/550	43
$SrWO_4$:Yb^{3+}/Er^{3+} MP	300–420	1.50% at 403 K	$866/T^2$	525/547	51
Er^{3+}/Yb^{3+}:GdOF@SiO_2 NP	260–490	0.98% at 490 K	$1087/T^2$	534/543	52
$NaGd(WO_4)_2$:Yb^{3+}/Er^{3+}@SiO_2 NP	300–350	1.03% at 350 K ($^2H_{11/2}$/$^4S_{3/2}$)	$1217/T^2$	531.5/553	This work
$NaGd(WO_4)_2$:Yb^{3+}/Er^{3+}@SiO_2 NP	300–350	2.14% at 350 K ($^2H_{11/2}$/$^4F_{9/2}$)	$1217/T^2$	531.5/657	This work

The FIR increases from 2.18 (300 K) to 3.09 (350 K) as shown in Fig. 6b. The $^2H_{11/2}$/$^4F_{9/2}$ FIR values are higher than those of $^2H_{11/2}$/$^4S_{3/2}$ FIR. The corresponding S_A and S_R are plotted *versus* temperature in Fig. 6c and d. Similar to the case of $^2H_{11/2}$/$^4S_{3/2}$ FIR (1.03% K^{-1} at 350 K), here S_A (calculated as the first derivative of FIR respect to each temperature point) increases with temperature, but is higher (2.14% K^{-1} at 350 K). The red emitting $^4F_{9/2}$ level is thermally quenched by increasing temperature, similar to the green emitting $^4S_{3/2}$ level. In contrast, S_R also increases with temperature with the highest 0.70% K^{-1} at 345 K.

Thermal cycling experiments were measured to demonstrate the repeatability and accuracy of our FIR analysis based on the prepared core–shell UCNPs. FIR per cycle step is shown in Fig. 7. During different cycles of heating and cooling, FIR fluctuates slightly, verifying the reliability of ratiometric technique.

Finally, thermal sensitivity is compared for the core–shell NGW:Yb^{3+}/Er^{3+}@SiO_2 UCNPs and other Yb^{3+} and Er^{3+} co-doped materials, as summarized in Table 1. The results of comparison demonstrate that the prepared core–shell NGW:Yb^{3+}/Er^{3+}@SiO_2 UCNPs in this work is a good candidate for biological nano-thermometry based on the FIR analysis of thermally coupled and non-thermally coupled levels.

4. Conclusions

In summary, uniformly dispersed NGW:Yb^{3+}/Er^{3+} core and NGW:Yb^{3+}/Er^{3+}@SiO_2 core–shell UCNPs have been successfully synthesized using the ethylene glycol-assistant hydrothermal method and the Stöber method for silica coating. The silica shell is homogeneously coated on the surface of the core NGW:Yb^{3+}/Er^{3+} UCNPs. Through silica coating, the stability of UCNPs was improved and provides more options in surface functionalization without damaging UC emission. After thermal treatments, the UCNPs can have relatively strong green and red UC emission involving two- and three-photons absorption and energy transfer. Temperature-dependent UC emission spectra were measured in the small biological temperature range and analyzed based on the FIR technique of the $^2H_{11/2}$ level to the thermally coupled $^4S_{3/2}$ level and the non-thermally coupled $^4F_{9/2}$ level. The maximum S_A is ~2-fold enhanced through the silica coating. A high absolute sensitivity of 2.14% K^{-1} at 350 K can be realized by FIR analysis of the unconventional $^2H_{11/2}$ and $^4F_{9/2}$ levels. The study demonstrates that the core–shell NGW:Yb^{3+}/Er^{3+}@SiO_2 UCNPs can be promising in nano-thermometry for the biological systems with proper size control and surface engineering.

Conflicts of interest

There are no conflicts to declare.

Acknowledgements

This work was financially supported by the National Natural Science Foundation of China (grant no. 21771196).

References

1 B. Ding, S. Shao, C. Yu, B. Teng, M. Wang, Z. Cheng, K. Wong, P. Ma and J. Lin, *Adv. Mater.*, 2018, **30**, 1802479.
2 C. Hsu, S.-L. Lin and C. A. Chang, *ACS Appl. Mater. Interfaces*, 2018, **10**, 7859–7870.
3 H. Dong, S. Du, X. Zheng, G. Lyu, L. Sun, L. Li, P. Zhang, C. Zhang and C. Yan, *Chem. Rev.*, 2015, **115**, 10725–10815.
4 A. Karnkaew, F. Chen, Y. Zhan, R. L. Majewski and W. Cai, *ACS Nano*, 2016, **10**, 3918–3935.
5 M. Haase and H. Schafer, *Angew. Chem., Int. Ed.*, 2011, **50**, 5808–5829.
6 F. Vetrone, R. Naccache, A. Zamarron, A. Juarranz de la Fuente, F. Sanz-Rodriguez, L. Martinez Maestro, E. Martin Rodriguez, D. Jaque, J. Garcia Sole and J. A. Capobianco, *ACS Nano*, 2010, **4**, 3254–3258.
7 L. Liu, L. Cheng, B. Chen, J. Shang, X. Qi, Y. Zhu and R. Hua, *J. Alloys Compd.*, 2018, **741**, 927–936.
8 H. Zheng, B. Chen, H. Yu, J. Zhang, J. Sun, X. Li, M. Sun, B. Tian, S. Fu, H. Zhong, B. Dong, R. Hua and H. Xia, *J. Colloid Interface Sci.*, 2014, **420**, 27–34.
9 L. Mukhopadhyay and V. K. Rai, *New J. Chem.*, 2017, **41**, 7650–7661.
10 X. Zhu, J. Li, X. Qiu, Y. Liu, W. Feng and F. Li, *Nat. Commun.*, 2018, **9**, 2176.

11 T. Li, C. Guo, S. Zhou, C. Duan, M. Yin and H. Hintzen, *J. Am. Ceram. Soc.*, 2015, **98**, 2812–2816.
12 A. Dong, X. Ye, J. Chen, Y. Kang, T. Gordon, J. M. Kikkawa and C. B. Murray, *J. Am. Chem. Soc.*, 2011, **133**, 998–1006.
13 C. Cascales, C. L. Paino, E. Bazan and C. Zaldo, *Nanotechnology*, 2017, **28**, 185101.
14 G. Gao, D. Busko, S. Kauffmann-Weiss, A. Turshatov, I. A. Howard and B. S. Richards, *J. Mater. Chem. C*, 2017, **5**, 11010–11017.
15 Z. Wang, J. Christiansen, D. Wezendonk, X. Xie, M. A. van Huis and A. Meijerink, *Nanoscale*, 2019, **11**, 12188–12197.
16 F. Artizzu, D. Loche, D. Mara, L. Malfatti, A. Serpe, R. Van Deun and M. F. Casula, *J. Mater. Chem. C*, 2018, **6**, 7479–7486.
17 X. Xu, W. Li, W. Zhou, G. Tan, Y. Zheng, C. Hu, B. Lei, X. Zhang, Y. Liu and J. Zhuang, *J. Mater. Chem. C*, 2018, **6**, 10360–10366.
18 A. El-Toni, M. Habila, J. Labis, Z. ALOthman, M. Alhoshan, A. Elzatahry and F. Zhang, *Nanoscale*, 2016, **8**, 2510–2531.
19 M. Ocana, E. Cantelar and F. Cusso, *Mater. Chem. Phys.*, 2011, **125**, 224–230.
20 L. Liu, H. Xiao, X. An, Y. Zhang, R. Qin, L. Liu, D. Zhang, R. Sun and L. Chen, *Chem. Phys. Lett.*, 2015, **619**, 169–173.
21 D. Yang, C. Cao, W. Feng, C. Huang and F. Li, *J. Rare Earths*, 2018, **36**, 113–118.
22 A. Ansari, A. Khan, J. Labis, M. Alam, M. Aslam Manthrammel, M. Ahamed, M. Akhtar, A. Aldalbahi and H. Ghaithan, *Mater. Sci. Eng., C*, 2019, **96**, 365–373.
23 F. Chen, C. Yang, X. Liu, N. Zhang, P. Rong, S. Liang and R. Ma, *ACS Sustainable Chem. Eng.*, 2018, **6**, 10463–10471.
24 T. Zhao, N. Goswami, J. Li, Q. Yao, Y. Zhang, J. Wang, D. Zhao and J. Xie, *Small*, 2016, **12**, 6537–6541.
25 M. Gnanasammandhan, N. Idris, A. Bansal, K. Huang and Y. Zhang, *Nat. Protoc.*, 2016, **11**, 688–713.
26 K. Li, D. Zhu and H. Lian, *J. Alloys Compd.*, 2020, **816**, 152554.
27 Y. Zhu, Q. Meng, W. Sun and S. Lu, *J. Lumin.*, 2020, **218**, 116854.
28 Z. Zou, T. Wu, H. Lu, Y. Tu, S. Zhao, S. Xie, F. Han and S. Xu, *RSC Adv.*, 2018, **8**, 7679–7686.
29 R. Geitenbeek, P. Prins, W. Albrecht, A. van Blaaderen, B. Weckhuysen and A. Meijerink, *J. Phys. Chem. C*, 2017, **121**, 3503–3510.
30 G. Xiang, X. Liu, J. Zhang, Z. Liu, W. Liu, Y. Ma, S. Jiang, X. Tang, X. Zhou, L. Li and Y. Jin, *Inorg. Chem.*, 2019, **58**, 8245–8252.
31 J. Liao, L. Nie, Q. Wang, S. Liu, H.-R. Wen and J. Wu, *RSC Adv.*, 2016, **6**, 35152–35159.
32 J. Gu, Y. Zhu, H. Li, X. Zhang and Y. Qian, *J. Solid State Chem.*, 2010, **183**, 497–503.
33 A. Kaminskii, H. Eichler, K. Ueda, N. Klassen, B. Redkin, L. Li, J. Findeisen, D. Jaque, J. Garcia-Sole, J. Fernandez and R. Balda, *Appl. Opt.*, 1999, **38**, 4533–4547.
34 M. Mahata, K. Kumar and V. Rai, *Spectrochim. Acta, Part A*, 2014, **124**, 285–291.
35 J. van Hest, G. A. Blab, H. C. Gerritsen, C. D. Donega and A. Meijerink, *J. Phys. Chem. C*, 2017, **121**, 19373–19382.
36 X. Ge, L. Sun, B. Ma, D. Jin, L. Dong, L. Shi, N. Li, H. Chen and W. Huang, *Nanoscale*, 2015, **7**, 13877–13887.
37 H. Ding, Y. Zhang, S. Wang, J. Xu, S. Xu and G. Li, *Chem. Mater.*, 2012, **24**, 4572–4580.
38 R. Calderon-Villajos, C. Zaldo and C. Cascales, *Nanotechnology*, 2012, **23**, 505205.
39 M. Lin, L. Xie, Z. Wang, B. S. Richards, G. Gao and J. Zhong, *J. Mater. Chem. C*, 2019, **7**, 2971–2977.
40 J. Boyer, M. Manseau, J. Murray and F. van Veggel, *Langmuir*, 2010, **26**, 1157–1164.
41 Z. Wang and A. Meijerink, *J. Phys. Chem. C*, 2018, **122**, 26298–26306.
42 F. Rabouw, P. Prins, P. Villanueva-Delgado, M. Castelijns, R. Geitenbeek and A. Meijerink, *ACS Nano*, 2018, **12**, 4812–4823.
43 O. A. Savchuk, J. J. Carvajal, C. Cascales, M. Aguilo and F. Diaz, *ACS Appl. Mater. Interfaces*, 2016, **8**, 7266–7273.
44 L. Marciniak, K. Prorok, L. Frances-Soriano, J. Perez-Prieto and A. Bednarkiewicz, *Nanoscale*, 2016, **8**, 5037–5042.
45 E. C. Ximendes, W. Q. Santos, U. Rocha, U. K. Kagola, F. Sanz-Rodriguez, N. Fernandez, A. d. S. Gouveia-Neto, D. Bravo, A. M. Domingo, B. del Rosal, C. D. S. Brites, L. D. Carlos, D. Jaque and C. Jacinto, *Nano Lett.*, 2016, **16**, 1695–1703.
46 G. Xiang, X. Liu, J. Zhang, Z. Liu, W. Liu, Y. Ma, S. Jiang, X. Tang, X. Zhou, L. Li and Y. Jin, *Inorg. Chem.*, 2019, **58**, 8245–8252.
47 Y. Ma, G. Xiang, J. Zhang, Z. Liu, P. Zhou, W. Liu, X. Tang, S. Jiang, X. Zhou, L. Li, Y. Luo and Y. Jin, *J. Alloys Compd.*, 2018, **769**, 325–331.
48 P. Du, L. Luo, H.-K. Park and J. S. Yu, *Chem. Eng. J.*, 2016, **306**, 840–848.
49 M. Runowski, N. Stopikowska, D. Szeremeta, S. Goderski, M. Skwierczynska and S. Lis, *ACS Appl. Mater. Interfaces*, 2019, **11**, 13389–13396.
50 J. Cao, F. Hu, L. Chen, H. Guo, C. Duan and M. Yin, *J. Am. Ceram. Soc.*, 2017, **100**, 2108–2115.
51 A. Pandeya, V. K. Rai, V. Kumar, V. Kumar and H. C. Swart, *Sens. Actuators, B*, 2015, **209**, 352–358.
52 H. Suo, X. Zhao, Z. Zhang and C. Guo, *ACS Appl. Mater. Interfaces*, 2017, **9**, 43438–43448.